Electronic Supplementary Information

An Efficient and Durable Anode for Ammonia Protonic Ceramic Fuel Cells

Hua Zhang[1□], Yucun Zhou[2□], Kai Pei[1], Yuxin Pan[1], Kang Xu[1], Yong Ding[2], Bote Zhao[1], Kotaro Sasaki[3], YongMan Choi[4*], Yu Chen[1*] and Meilin Liu[2*]

[1]School of Environment and Energy, South China University of Technology, Guangzhou, 510006, China

[2]School of Material Science and Engineering, Georgia Institute of Technology, Atlanta, GA 30309, US

[3]Chemistry Department, Brookhaven National Laboratory, Upton, NY 11973, USA

[4]College of Photonics, National Yang Ming Chiao Tung University, Tainan 71150, Taiwan

□These authors contribute equally.

*Corresponding authors:

YongMan Choi (ymchoi@nctu.edu.tw);

Yu Chen (eschenyu@scut.edu.cn);

Meilin Liu (Meilin.liu@mse.gatech.edu).

Experimental section

Preparation of $PrBa_{0.5}Sr_{0.5}Co_{1.5}Fe_{0.5}O_{5+\&}$（PBSCF）powder

PBSCF power was prepared by a citric nitrate solution combustion method. Stoichiometric amounts of $Pr(NO_3)_3$, $Ba(NO_3)_2$, $Sr(NO_3)_2$, $Co(NO_3)_2 \cdot 6H_2O$,Fe $(NO_3)_3 \cdot 9H_2O$, were dissolved in DI water to form a solution of $PrBa_{0.5}Sr_{0.5}Co_{1.5}Fe_{0.5}O_{5+\&}$. A sichiometric amounts of ctric acid (CA) and glycine were added as the complexing agent and the fuel for subsequent self-combustion. Metal ions: CA: glycine of 1: 0.75: 0.75. The power was then fired at 900 ^oC for 2 h.

Fabrication of single cells

The NiO/BZCYYb anode supported half-cells were prepared by tape casting and co-sintering. The electrolyte slurry, anode functional layer slurry and anode slurry were casted sequentially onto a polymer film. After drying in air for 15 hours, the tape was punched into pellets and then pre-heated at 600^oC for 2 hours. In the pre-heating process, a slow heating rate was applied so that all the organic components with the pellets can be removed without destroying the pellets. Finally, the pellets with three-layered structure (anode support layer, anode functional layer and electrolyte) were co-sintered at 1450^oC for 5 hours to form anode supported half cells. PBSCF cathode was screen-printed onto the surface of BZCYYb electrolyte. The cells were then co-fired at 950 ^oC for 2h to form porous hybrid cathode (with an area of 0.2826 cm^2).

Catalytic test for Ni/BZCYYb powder

The catalytic activity of Ni/BZCYYb powder was carried out on a continuous fixed-bed quartz reactor (catalyst: 0.3 g, 10-15 mesh) under pure NH_3 with a flow rate of 30 mL min^{-1}. Firstly, the powder of Ni/BZCYYb catalysts was heated to 700^oC in an Ar flow (50 mL min^{-1}) with a heating rate of 5^oC min^{-1} and followed by reducing at 700^oC for 2 h in 50% H_2-50% At at a flow rate of 100 mL min^{-1}. Then, the gas was switched to NH_3 (30 mL min^{-1}) and the catalysts were heated in the range of 350-750^oC. The measurement of effluent gas was introduced to a sulfuric acid aqueous solution to remove unreacted ammonia and analyzed using on-line gas chromatograph (GC-7820, Shimadzu) equipped with a thermal conductivity cell detector (TCD). The conversion

of ammonia was calculated by the following Eq. (4)

$$NH_3\ conversion = \left(1 - \frac{n_{NH_3 outlet}}{n_{NH_3 inlet}}\right) \times 100\% \quad (4)$$

where $n_{NH_3 outlet}$ and $n_{NH_3 outlet}$ are the molar ratio of outlet and inlet ammonia, respectively. During the ammonia decomposition processing, the space velocity of reactant gas was set as 6000 L kg^{-1} h^{-1}.

Electrochemical Measurements

The Ni-BZCYYb/BZCYYb/PBSCF single-cell was placed in a furnace of the test rig. For electrochemical testing, the electrode surface was partially connected with Ag mesh by using Ag paste (DAD-87, purchased from Shanghai Synthetic Resin Research Institute). Prior to electrochemical test, the single-cell was heated to 700°C in ambient air, followed by the reduction of anode in 3 % humidifified H_2 (~3 % H_2O) at a flow rate of 30 mL min^{-1}, composite cathode was exposed to ambient air. Then the anode was supplied by NH_3 at a flow rate of 20 mL min^{-1}. The single cell was operated in a temperature range of 550 °C to 700 °C

The open-circuit voltage (OCV), current–voltage (*I-V*) and impedance spectra characteristics of single cell fueled with hydrogen and ammonia were measured by using electrochemical workstation (AMETEK PARSTAT MC). For the long-term stability tests of the NH_3-fueled SOFC, the cell was discharged at 0.5 A cm^{-2}. The frequency range for all impedance measurements was between 100 mHz and 10 kHz with an AC amplitude of 10 mV.

Characterization

The microscopic morphology analysis of the cell was performed using a thermal field emission scanning electron microscope (SEM, Hitachi SU8010, Japan) or a transmission electron microscope equipped with energy-dispersive spectrum analysis (JEOL 4000EX). A standard cross-section sample preparation routine was followed for preparation of the TEM samples. Specifically, bulk samples were cut into rectangle pieces (2.2 mm×1.5 mm) and then attached face-to-face together by the conductive epoxy. Then the two sides of samples were mechanical polished down to 100 μm,

followed by dimpling to 20 μm. Then sample was transferred onto a Cu ring and ion milled to open a hole in the middle. The crystal structures of the as-synthesized Ni/BZCYYb and after10μL of 0.1M $Fe(NO_3)_3$ infiltration exposure at 700 °C for 1 h were measured by X-ray diffractometer (Rigaku, Miniflex model) with Cu Ka radiation at room temperature.

Computational methods

All of the spin-polarized density functional theory (DFT) calculations were executed using the Vienna Ab initio Simulation Package (VASP)[1, 2]. We applied Perdew-Burke-Ernzerh (PBE) functional[3] with the projector augmented plane wave (PAW) method[4] to systematically deal with the enhanced performance of the NH_3-fueled protonic ceramic fuel cell using Fe-modified Ni/BZCYYb compared to Ni/BZCYYb anodes. For the NH_3 decomposition processes, (3 × 3) surfaces of Ni (111) (36 Ni atoms) and FeNi (111) (1 Fe and 35 Ni atoms) were applied (*i.e.*, coverage of 1/9). Besides, similar to the previous studies of CeO_2, $BaCeO_3$, $BaZr_{0.7}Ce_{0.1}Y_{0.1}Yb_{0.1}O_3$[5, 6], the PBE + U method was applied with U_{eff} = 5.0 eV for accurately describing the strong on-site Coulomb repulsion of the Ce 4f electrons to model $BaZr_{0.7}Ce_{0.1}Y_{0.1}Yb_{0.1}O_3$ (Ba_{10}-$Zr_7Ce_1Y_1Yb_1O_{30}$). The reaction pathways of the NH_3 decomposition on FeNi (111) and Ni (111) and the incorporation of surface hydrogen species into BZCYYb (001) were examined by using the climbing-image nudged elastic band (CI-NEB) method[7]. Its microkinetic modeling was carried out using the MKMCXX software package[8] at T = 700°C. The detailed information about the computational study can be found in Supplementary Note 14 and 15.

Supplementary Note 1

The pore information of the anode

The anode of our anode supported PCFC consists of two layers **(Supplementary Figure S1**): anode functional layer (AFL, ~20 μm) and anode supporting layer (ASL, ~800 μm). The AFL has finer pores and larger surface area (due mainly to the reduction of NiO), providing more triple phase boundaries for electrochemical reactions. In contrast, the AFL has larger pores and continuous channels (due mainly to the removal of pore-former), providing facile paths for gas transport.

Supplementary Note 2

Catalyst performance of the commercial Ni-yttria-stabilized zirconia (Ni-YSZ) power and the Ni-BZCYYb power used in this study

The ammonia conversion rate on these two powders increases significantly with the rising of temperature. At each temperature, the Ni/BZCYYb exhibited higher activity for ammonia decomposition than Ni/YSZ did. At 650^{o}C (close to operating temperature), the activity reaches ~100% over Ni-BZCYYb, while the ammonia conversion over Ni–YSZ was about 79%. Thus, it is suggested that proton-conductor based anode showed a higher activity toward ammonia decomposition. The results were shown in **Supplementary Figure S2**.

Supplementary Note 3

The structure evolution of anode before and after modification

The anode surface was modified via a solution infiltration process. Specifically, $Fe(NO_3)_3{\cdot}6H_2O$ was dissolved in deionized water to prepare the 0.1 M $Fe(NO_3)_3{\cdot}6H_2O$ precursor solution. The surfactant PVP (5wt %) was added into the 0.1 M $Fe(NO_3)_3{\cdot}6H_2O$ precursor solution to improve the wetting/penetration of the solution, thus ensuring a uniform dispersion of infiltrate. The $Fe(NO_3)_3{\cdot}6H_2O$ solution was then dropped onto the surface of the sintered NiO-BZCYYb backbone and spread over the entire anode surface. The solution was sucked into the pores of the backbone, driven by

capillary forces. The infiltrated samples were then fired at 700 °C in H_2 for 3 h with a heating/cooling rate of 5 °C min^{-1}. The loading of catalyst was measured after the heat treatment and increased by repeating the infiltration process. Shown in **Supplementary Figure S3** are the typical SEM images of anode surfaces before (**Supplementary Figure S3a-c)** and after (**Supplementary Figure S3d-f)** modification with catalysts. As observed, the nanoparticles are preferentially deposited on the surface of Ni grain

Supplementary Note 4

XRD analysis and TEM images of the Fe-modified Ni-BZCYYb anode

Fe and Ni are close to each other in the periodic table. Accordingly, they follow the Hume-Rothery rule very well; a solid solution of Fe-Ni (alloy) can be readily formed. Under our experimental conditions, it is also suggested that an alloy with a possible composition of $FeNi_3$ is formed, which can be supported by the XRD of anodes after testing (**Supplementary Figure S4**) and the zoomed-in lattice parameters of the coatings on Ni surface (**Supplementary Figure S5**). The interplanar spacing of the surface coating is ~0.177 nm, which might be corresponding to the (200) plane of the $FeNi_3$ alloy (PDF#38-0419).

Supplementary Note 5

XPS analysis of the Fe-modified Ni-BZCYYb anode

The electronic states of Fe-modified Ni/BZCYYb anode were further characterized by high resolution XPS (**Supplementary Figure S6**). All the binding energy scales are calibrated using the C 1 s peak with a binding energy of 284.8 eV. The high-resolution Fe 2p spectrum of Fe-modified Ni/BZCYYb (**Supplementary Figure S6a**) can be fitted by four deconvolution peaks. The peak at 706.8 eV is attributed to the Fe $2p^{3/2}$ of Fe metal. The peaks at 710.7 eV and 723.6 eV are related to Fe $2p_{3/2}$ and Fe $2p_{1/2}$ of Fe^{3+} states from oxidation of the surface, respectively[9]. The peak at 715.8 eV is the corresponding satellite feature of Fe^{3+} [10]. In the high-resolution Ni 2p spectrum of Fe-modified Ni/BZCYYb (**Supplementary Figure S6b**), four deconvolution peaks can be obtained. The peaks at 852.3 and 869.6 eV correspond to

the Ni $2p_{3/2}$ and Ni $2p_{1/2}$ of Ni metal, respectively. The two peaks show a spin–orbit splitting of 17.3 eV, which further indicates the presence of Ni metal in the samples. The peaks at 855.5 eV and 873.3 eV can be ascribed to the Ni $2p_{3/2}$ and Ni $2p_{1/2}$ of Ni^{2+} states respectively[11]. Combined the XPS and XRD results (**Supplementary Figure S4**), Ni electronic structures change with the incorporation of Fe, and the metallic Ni and Fe would be compounded to Fe-Ni alloy NPs. Because no any obvious Ni- or Fe-oxides are observed from the XRD patterns (**Supplementary Figure S4**), it suggests that the detected signals of Ni^{2+} and Fe^{3+} might be ascribed to the slightly oxidization shells on their surfaces[10, 11].

Supplementary Note 6

The *IVP* curves of the cells with bare Ni/BZCYYb anode and Fe-modified Ni/BZCYYb anode at 650°C when wet H_2 (with 3% humidity) and dry NH_3 were used as the fuel

Shown in **Supplementary Figure S7a** and **S7c** are the *IVP* curves of the cells with bare Ni/BZCYYb anode at 650°C when wet H_2 (with 3% humidity) and dry NH_3 were used as the fuel. Shown in **Supplementary Figure S7b** and **S7d** are the *IVP* curves of the cells with Fe-modified Ni/BZCYYb anode at 650°C when wet H_2 (with 3% humidity) and dry NH_3 were used as the fuel. The *IVP* curves shown in each figure were obtained from three different cells fabricated using identical procedures (with the same materials and cell configuration). The OCV values for all three cells on wet H_2 (3% humidity) with bare Ni-BZCYYb anode is about 1.039 V; the peak power density is about 1.15 Wcm^{-2}. The OCV values for all three cells on dry ammonia with Fe-Ni-BZCYYb anode are about 0.99 V; the peak power density is about 1.25 Wcm^{-2}. It is suggested that our cell shows a good reproducibility (seen in **Supplementary Table S1**), which is likely attributed to the robust cell fabrication procedures such as tape-casting, co-sintering, and screen-printing. The thickness and porosity of each functional layer (anode, cathode, and electrolyte) remain essentially the same for each batch of cells.

Supplementary Note 7

The possibilities for the reasons of the increase in ohmic resistance of the cell when NH_3 is supplied, compared with that in H_2: the change of hydrogen partial pressure (p_{H2}) caused by the NH_3 decomposition

In this study, H_2 and NH_3 is supplied to the fuel cell at a flow rate of 30 sccm, and 20 sccm, respectively. Under typical fuel cell operation condition, NH_3 is completely converted to H_2 and N_2 ($NH_3 \rightarrow 1/2\ N_2 + 3/2\ H_2$). Then the hydrogen partial pressure (p_{H_2}) in the anode of the NH_3 cell decreased to 0.75 compared to that of the H_2 cell. To investigate whether the hydrogen partial pressure (p_{H_2}) can cause the increase in ohmic resistance when NH_3 is supplied, we tested the cells with simulated N_2/H_2 with p_{H2} of 1, 0.8, 0.6, 0.4, and 0.21 (balanced with N_2). As seen in **Supplementary Figure S8**, the ohmic resistance (R_{ohm}) increases as the hydrogen partial pressure (p_{H_2}) decreases. Compare with that in pure H_2 (p_{H2}=1), R_{ohm} values are increased by 2.98 % and 9.95 % when tested in hydrogen at a p_{H_2} of 0.8 and 0.6 at 650°C. At the same time, an ohmic resistance change of 8.59 % is observed when the fuel was switched from pure H_2 (p_{H2}=1) to NH_3 (p_{H2}=0.75) at 650°C. This finding is consistent with the one reported by Aoki et al. In that study, the power output of NH_3 cell is identical to that of H_2 cell using H_2 gases at p_{H_2}= 0.6 in the anode[12]. It may suggest that the ohmic resistance increase in our study can be attributed to the hydrogen partial pressure change when NH_3 is used as fuel.

Supplementary Note 8

Arrhenius plot of the electrode polarization resistance (R_p) and R_{ohm} for the bare anode and Fe-modified Ni/BZCYYb anode, tested at 550–700 °C using ammonia as fuel and ambient air as oxidant.

The plot R_p and R_{ohm} versus temperature (550 °C-700°C) for the bare anode and Fe-modified Ni/BZCYYb anode when exposed to NH_3 fuel are shown in **Supplementary Figure S9**. The change of R_{ohm} is small but the decrease in R_p caused

by the Fe modification is significant, indicating that Fe modification can effectively accelerate the rate of anodic reactions, thus improving the cell performance.

Supplementary Note 9

The performance and short-term stability test (24h) of cells with Fe-modified anode at variable current density at 650 °C

Short-term stability test (24h) of the single cell with bare anode in NH_3 fuel at 650 °C at a variable current density from 0.5 A cm^{-2} to 1.25 A cm^{-2} were shown in **Supplementary Figure S10**. As the current density varied from 0.5 A cm^{-2} to 1.25 A cm^{-2}, the degradation of the cell at different current density was basically consistent, a slightly degradation was observable, which may be due to the increase of R_p (see **Supplementary Figure S10c)**.

Supplementary Note 10

SEM images of cells after long-term stability (~100h) testing

The SEM images of the outer surface of the Ni/BZCYYb anode before and after exposure to wet H_2 (3% humidity) for 100h are shown in **Supplementary Figure S11a and S11b.** There is no significant change in particle size of the Ni. However, after the treatment in ammonia for 100h, the Ni/BZCYYb anode grains in Figure **Supplementary Figure S11c** were apparently agglomerated and the surface became significantly rougher as compared to those in **Supplementary Figure S11a and S11b,** possibly because ammonia is a more-favorable reducing agent than hydrogen at the 650 °C target operating temperature, potentially leading to a damage of the nickel phase of the cermet fuel electrode, as well as device degradation. Similarly, this phenomenon is consistent with Zhu's recent report where NH_3-treatment of the NiO sample results in a more highly porous, heavily reduced Ni electrode morphology than seen with the H_2-treated NiO sample[13]. Moreover, results from the Fe-Ni-BZCYYb anode after tested on NH_3 at 650 °C for 100 h showed that the outer surface of the Fe-Ni-BZCYYb anode was smooth, and the Ni particles in **Supplementary Figure S11d** did not apparently change. These results strongly imply a surface restructuring of the state-of-the-art Ni

anode with Fe catalyst could provide a good thermo-mechanical stability and a superior antisintering capability.

Supplementary Note 11

XRD of the anode after long-term stability (~100h) testing

We characterized the anodes after long-term testing by XRD (**Supplementary Figure S12**) and found no nitride formation on both the bare anode and Fe-Ni/BZCYYb anode. Moreover, thermodynamic calculation indicates that formation of Ni_3N is highly unfavorable and therefore unlikely become a predominant phase under typical PCFC operation temperatures, as supported by Zhu et al[13]. On the other hand, the formation of nickel nitrides could be neglected (reduced to nickel) since ammonia conversion is nearly 100% for the Ni-BZCYYb anode at 650 ^{o}C.

Supplementary Note 12

Stability of fuel cell with Fe-modified Ni-BZCYYb anode with different Fe loading

The influence of Fe loading on the stability of the single cells with Fe decorated Ni/BZCYYb anode on NH_3 was investigated. The stability testing of the single cells on NH_3 with various Fe loading anode at 0.5 A cm^{-2} at 650 ^{o}C was displayed in **Supplementary Figure S13**. The deterioration rate decreased with the increasing of Fe content at first, and reached the minimum deterioration rate (around 0.0022 V h^{-1}) at the loading amount of 10μL (~0.36 mg cm^{-2}). Further increase in the Fe loading resulted in a poor performance and a much faster deterioration rate, which may be due to the fact that the active sites of Ni were covered with excess Fe species.

Supplementary Note 13

A list of studies which have reported long-term operations of SOFC on NH_3

The stability test of the NH_3-fueled SOFC is vital to practical applications. Listed in **Supplementary Table S3** are the long-term operations results of SOFC on NH_3 that have been reported. To date, efforts on the long-term stability of the PCFCs on NH_3 were limited, compared with those of O-SOFC on NH_3. Theoretically, a complete

ammonia conversion would yield a gas mixture of 75% H_2 and 25% N_2, which is the same compositions as the feed for the diluted hydrogen SOFC, does not cause additional degradation to the cell. Hagen et al reported that an O-SOFC with a 53 × 53 mm^2 footprint with ammonia fuel for 1,500 h at 850 °C and confirmed comparable stability of the performance to that with hydrogen fuel [14]. However, some groups have observed the performance degradation of O-SOFCs on NH_3, which has been ascribed to the anode degradation. There are two possible mechanisms for the anode degradation in the presence of ammonia. One is the nitridation of nickel catalyst in ammonia at low temperatures due to the incomplete ammonia conversion. Yang et al. observed that internal resistances increased and the support anode layer destructed when the cells with Ni/YSZ anodes fueled with humidified ammonia in a temperature range of between 600°C and 700°C[15]. The authors reported that the degradation is due to the formation of Ni_3N at low temperatures (600°C), caused by the undesired reaction of anode with the residual ammonia. However, the formation of nickel nitrides could be neglected (reduced to nickel) when the operation temperature is above 700 °C since nearly 100% ammonia conversion is achieved at 700°C. Thus, a good ammonia conversion of the anode of the SOFC is crucial to the stability. The other one is the microstructural change of the anode, such as the agglomeration, corrosion and porosity of Ni particles. In addition, the influence of the sealing materials, interconnects and piping materials on long lifespan of the SOFC under an NH_3 atmosphere cannot be ignored. M. Kishimoto et al reported that the 1000 h's long-term durability test of the stacks consisting of 30 planar anode-supported cells fueled with direct ammonia at 770 °C [16]. After the durability test, a nitride layer in the bulk and Fe-rich particles on the surface of the separator material (SUS430) were observed. Therefore, the issue of nitriding of the separator materials needs to be considered as a critical issue when SOFC stacks are operated with direct ammonia.

Although there have been a great number of reports investigating the long-term stability of O-SOFCs on NH_3, the stability test of the PCFCs on NH_3 were limited. Therefore, it is still unclear if the performance degradation mechanism mentioned above is applicable to the of PCFCs when fueled with ammonia. Zhu et al recently

suggested that the lower operating temperatures of PCFCs likely lead to different degradation mechanisms vs. NH_3-fed SOFCs[13]. They reported that the voltage dropped to zero after ~15 h of direct NH_3 exposure when using a PCFC with a ~500 μm thick porous Ni-BCZYYb cermet electrode support with a ~4 μm-thick dense BCZYYbN electrolyte ($BaCe_{0.7}Zr_{0.1}Y_{0.1}Yb_{0.1}Ni_{0.04}O_{3-\delta}$). The authors suggested that the BCZYYb electrolyte phase in the anode support (rather than the nickel phase) is mostly responsible for the fast PCFC degradation rate when operating under NH_3 fuel without ammonia cracking catalyst at 650 °C. However, in our study, the cell with the Fe decorated Ni/BZCYYb anode showed a slower deterioration rate (around 0.0022 V h^{-1}) than the one with the bare anode (around 0.008 V h^{-1}). The performance degradation rate of the cells on NH_3 is close to that of the cell on H_2. No significant change of Ni and BZCYYb particle sizes was observed after running on NH_3 for 100 h.

Supplementary Note 14

Density functional theory (DFT)-based calculations.

We performed spin-polarized periodic density functional theory (DFT) calculations by the plane-wave basis set with the projector augmented plane wave (PAW) method[17] as implemented in the Vienna Ab initio Simulation Package (VASP).[1, 2] We applied Perdew-Burke-Ernzerh (PBE) functional[3] with generalized gradient approximation (GGA) to systematically deal with the enhanced performance of the NH_3-fueled protonic ceramic fuel cell using Fe-modified Ni/BZCYYb compared to Ni/BZCYYb anodes. The plane-wave cutoff energy with 415 eV was employed. Brillouin-zone integrations were performed on grids of (3 × 3 × 3) and (3 × 3 × 1) **k**-point meshes with the Monkhorst–Pack method[18] for bulk and surface models, respectively. For the NH_3 decomposition processes, a bulk Ni model (cubic, $Fm\bar{3}$m) was prepared ($a_{,DFT}$ = 3.5156 Å) and cleaved for the (111) facet which is the densest plane among the low-index (111), (110), and (100) surfaces. In this study, to avoid the interaction between two slabs consisting of 4-atomic layers, a 15 Å of vacuum space was added. (3 × 3) surfaces of Ni (111) (36 Ni atoms) and FeNi (111) (1 Fe and 35 Ni atoms) were applied (*i.e.*,

coverage of 1/9). The dipole correction was always applied to remove artificial dipole interactions. For adsorption energy calculations, while the top two layers and adsorbates were allowed to fully relax, while its bottom two layers were fixed at the bulk properties. We first examined the most stable active sites of all of the surface species (*i.e.*, H*, N*, HN*, N_2N*, and H_3N*) both on Ni (111) and FeNi (111). Besides, similar to the previous studies of CeO_2, $BaCeO_3$, $BaZr_{0.7}Ce_{0.1}Y_{0.1}Yb_{0.1}O_3$,[5, 6] the PBE + U method was applied with U_{eff} = 5.0 eV for accurately describing the strong on-site Coulomb repulsion of the Ce 4f electrons. The optimized lattice constant of BZCYYb to reasonably model $BaZr_{0.7}Ce_{0.1}Y_{0.1}Yb_{0.1}O_3$ ($Ba_{10}Zr_7Ce_1Y_1Yb_1O_{30}$) ($a_{,DFT}$ = 4.4221 Å) was obtained using the bulk structure of $BaCeO_3$ (BCO, $Pm\bar{3}m$; 221) ($a_{,DFT}$ = 4.4705 Å) that is in good agreement with an experimental value ($a_{,expt.}$ = 4.4447 Å) and a theoretical result ($a_{,DFT}$ = 4.50 Å).[6] Then the BZCYYb(001) surface was chosen for surface calculations to investigate the adsorption of hydrogen species and incorporation into its bulk for proton transfer because we used the same structure of $BaCeO_3$ whose (001)-terminated surface has been used for DFT calculations due to its high stability.[19, 20] As shown **Supplementary Figure S14a**, the d-band centers are positively shifted by replacing the top-most Ni surface to Fe (Ni_4/Ni, Fe_1Ni_4/Ni, Fe_2Ni_2/Ni, Fe_3Ni_1/Ni, and Fe_4/Ni). Then, we noticed the adsorption energies of N* and HN* are linearly correlated as a function of d-band centers as shown below. The electronic structure calculations manifest that controlling the concentration of Fe on FeNi alloys is important to tune the energy of N adsorption in order to avoid the poison effect. The bulk structures and surface models used in this study are displayed in **Supplementary Figure S17**. The BZCYYb model is comprised of ten-atomic layers as summarized in **Supplementary Figure S17**. Similar to the surface calculations of the NH_3 decomposition on Ni(111) and FeNi(111), only the top five layers were fully relaxed, followed by surface stability calculations.[21] Using stable CeO-terminated surface models, defective structures were generated with one oxygen vacancy on its second layer ($BaZr_{0.7}Ce_{0.1}Y_{0.1}Yb_{0.1}O_{3-\delta}$; $Ba_{10}Zr_7Ce_1Y_1Yb_1O_{29}$) to fulfill the neutrality. The adsorption energies (E_{ads}) of X (X = H_3N*, H_2N*, HN*, N*, and H*) were calculated by E_{ads} = E(X-surface) – E(surface) –

E(X), where E(X-surface) and E(surface) are the calculated electronic energies for adsorbed X on a surface and its bare surface, respectively. E(X) is that for a gas-phase species (X = NH_3, NH_2, NH, N, and H). The reaction pathways of the NH_3 decomposition on FeNi(111) and Ni(111) and the incorporation of atomic hydrogen into BZCYYb(001) were accurately examined by using the climbing-image nudged elastic band method (CI-NEB).[7] Also, the interaction of adsorbates (N* and H_3N*) with (2 × 2) four-layer FeNi(111) was characterized by examining its d-band center (ε_d) according to the average energy of density of states (DOS) as follows.[22]

$$\varepsilon_d = \frac{\int E\rho_d(E)dE}{\int \rho_d(E)dE}$$

E and ρ_d are the energy and the density of d-electron, respectively.

Supplementary Note 15

Microkinetic modeling.

Microkinetic modeling of the NH_3 decomposition was carried out using the MKMCXX software package.[8] As shown below, we used the transition state theory (TST) formalism[23] to predict pre-exponential factors (A_i) for elementary steps with a well-defined reaction barrier for calculating rate constants at 700°C, while the canonical transition state theory (CVTST) approach[24, 25] was employed to approximate transition states for the adsorption step of NH_3 taking place without a barrier (variational processes).

$$k_i = A_i exp\left(-\frac{E_a}{k_B T}\right)$$

where k_i is a rate constant (s^{-1}), E_a is a zero-point energy (ZPE) corrected reaction barrier (eV) located using the CI-NEB approach, k_B is the Boltzmann constant, and T is temperature (K). ZPEs are calculated by $E_{ZPE} = \sum_{i=1}^{n} \frac{1}{2} h\nu_i$ where h and ν are the Planck constant and vibrational frequency, respectively. Vibrational frequencies were

calculated using VASP. To make the stoichiometric chemistry reasonable, we scaled the estimated consumption rates of NH_3 by comparing with the NH_3 fuel utilization (~17%) (**Supplementary Note 16**) after calculation the production rates (**Supplementary Figure S16b**). It is noted that the surface diffusion barriers of Ni (111) and FeNi (111) are relatively low compared to the dehydrogenation processes (0.12 eV versus 0.13 eV, respectively.

Supplementary Note 16

Evaluation of NH_3 utilization rate for fuel cell operation at 0.5 A/cm^2 or 0.5 V

When the fuel cell (with active electrode area of 0.2826 cm^2) is operated at a constant current density of 0.5 A/cm^2, the total current passing through the cell is 0.14 A (= 0.2826 cm^2 x 0.5Acm^{-2}). Thus, the rate at which electrons are pumped from the anode to the cathode of the cell would approximately be

$$\frac{i}{2F} = \frac{0.14C/s}{2 \times 96485C/mol} = 7.26 \times 10^{-7}\frac{mol}{s} = 4.36 \times 10^{-5}mol/min$$

If NH_3 is mainly conversion to H_2 and N_2 (2/3 $NH_3 \rightarrow$ 1/3 N_2 + 2 H^+ + 2 e^-), the corresponding ammonia consumption rate would be:

$$4.36 \times \frac{2}{3} \times \frac{10^{-5}mol}{min} = 2.91 \times 10^{-5}mol/min$$

On the other hand, ammonia is supplied to the fuel cell at a flow rate of 20 sccm, corresponding to

$$20\ sccm = 20 \times \frac{10^{-3}L}{min} = 20 \times \frac{10^{-3}mol}{22.4\ min} = 8.93 \times 10^{-4}\ mol/min$$

Therefore, the actual utilization/conversion rate of ammonia in the fuel cell under the fuel cell operating conditions would be ~3.3%

$$\frac{NH_3\ consumption\ rate}{NH_3\ supply\ rate} = \frac{2.91 \times 10^{-5}\ mol/min}{8.93 \times 10^{-4}\ mol/min} \approx 3.3\%$$

When the fuel cell with Fe decorated Ni/BZCYYb anode is operated under a voltage of 0.5 V, the experimentally measured total current passing through the cell is 0.76 A (= 0.2826 cm^2 x 2.7Acm^{-2}, see **Fig.2c**). Thus, the rate at which electrons are

pumped from the anode to the cathode of the cell would approximately be

$$\frac{i}{2F} = \frac{0.76\ C/s}{2 \times 96485 C/mol} = 3.94 \times 10^{-6} \frac{mol}{s} = 2.36 \times 10^{-4} mol/min$$

If NH_3 is mainly conversion to H_2 and N_2 (2/3 $NH_3 \rightarrow$ 1/3 N_2 + 2 H^+ + 2 e^-), the corresponding ammonia consumption rate would be:

$$2.36 \times \frac{2}{3} \times \frac{10^{-4} mol}{min} = 1.57 \times 10^{-4} mol/min$$

On the other hand, ammonia is supplied to the fuel cell at a flow rate of 20 sccm, corresponding to

$$20\ sccm = 20 \times \frac{10^{-3} L}{min} = 20 \times \frac{10^{-3} mol}{22.4\ min} = 8.93 \times 10^{-4}\ mol/min$$

Therefore, the actual utilization/conversion rate of ammonia in the fuel cell under the fuel cell operating conditions would be ~17%

$$\frac{NH_3\ consumption\ rate}{NH_3\ supply\ rate} = \frac{1.57 \times 10^{-4}\ mol/min}{8.93 \times 10^{-4}\ mol/min} \approx 17\%$$

Supplementary Figures

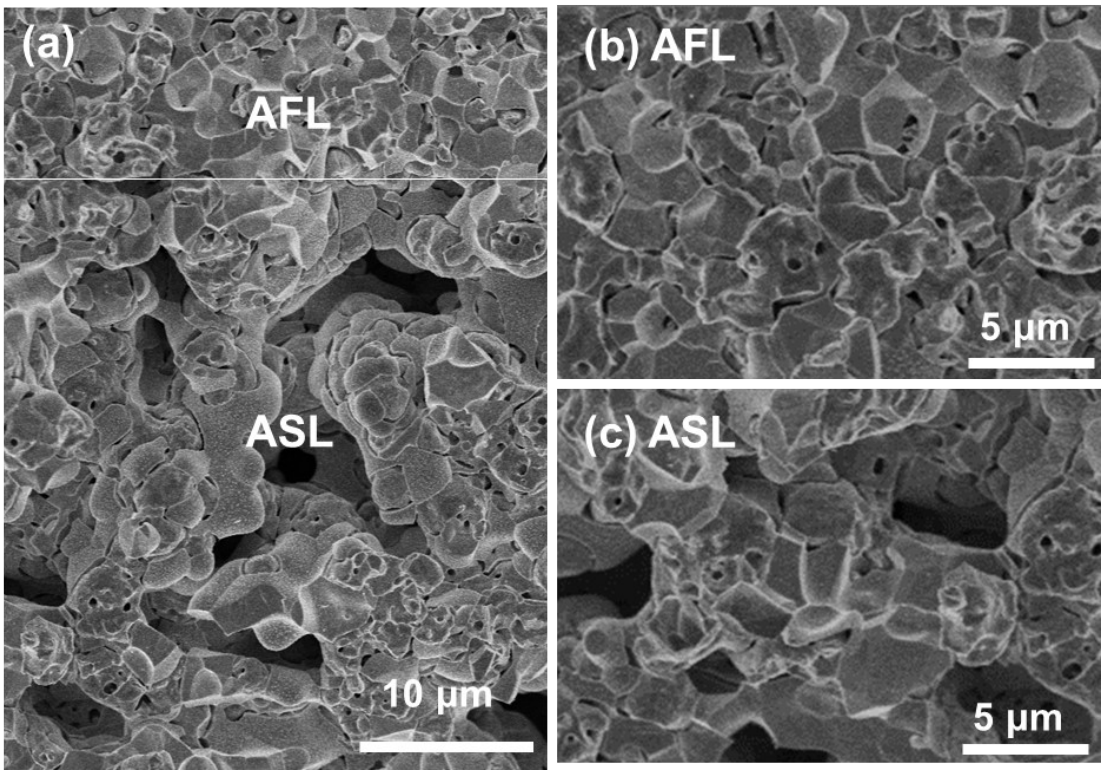

Supplementary Figure S1. Typical SEM image of the (a) anode layer; (b) anode functional layer (AFL) (c) and anode supporting layer (ASL) after reduction at 700°C in H_2 for 1 h.

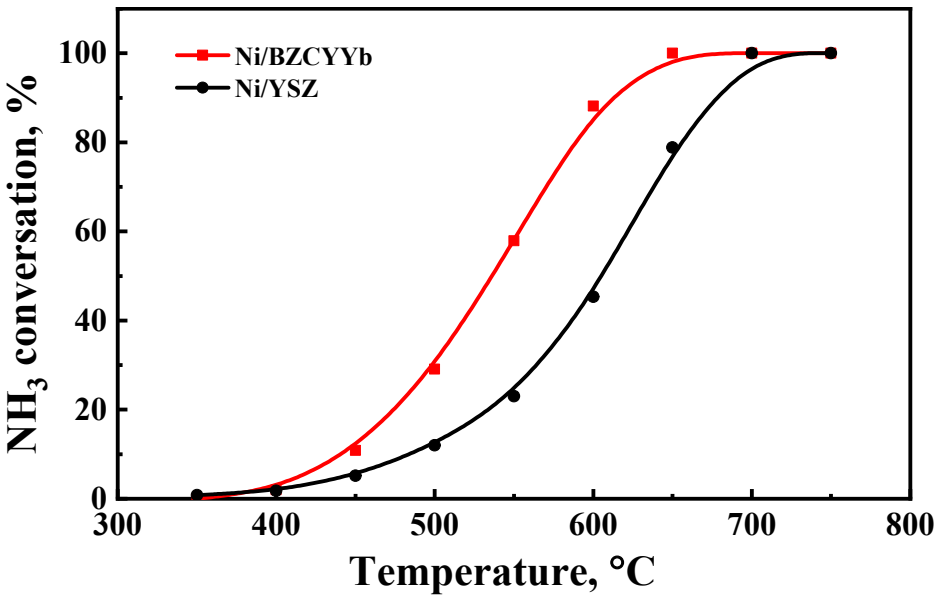

Supplementary Figure S2. Ammonia conversion over Ni/BZCYYb and Ni/YSZ. Reactant gases: 66.7% NH_3–33.3% N_2, gas space velocity: 6000 L kg^{-1} h^{-1}.

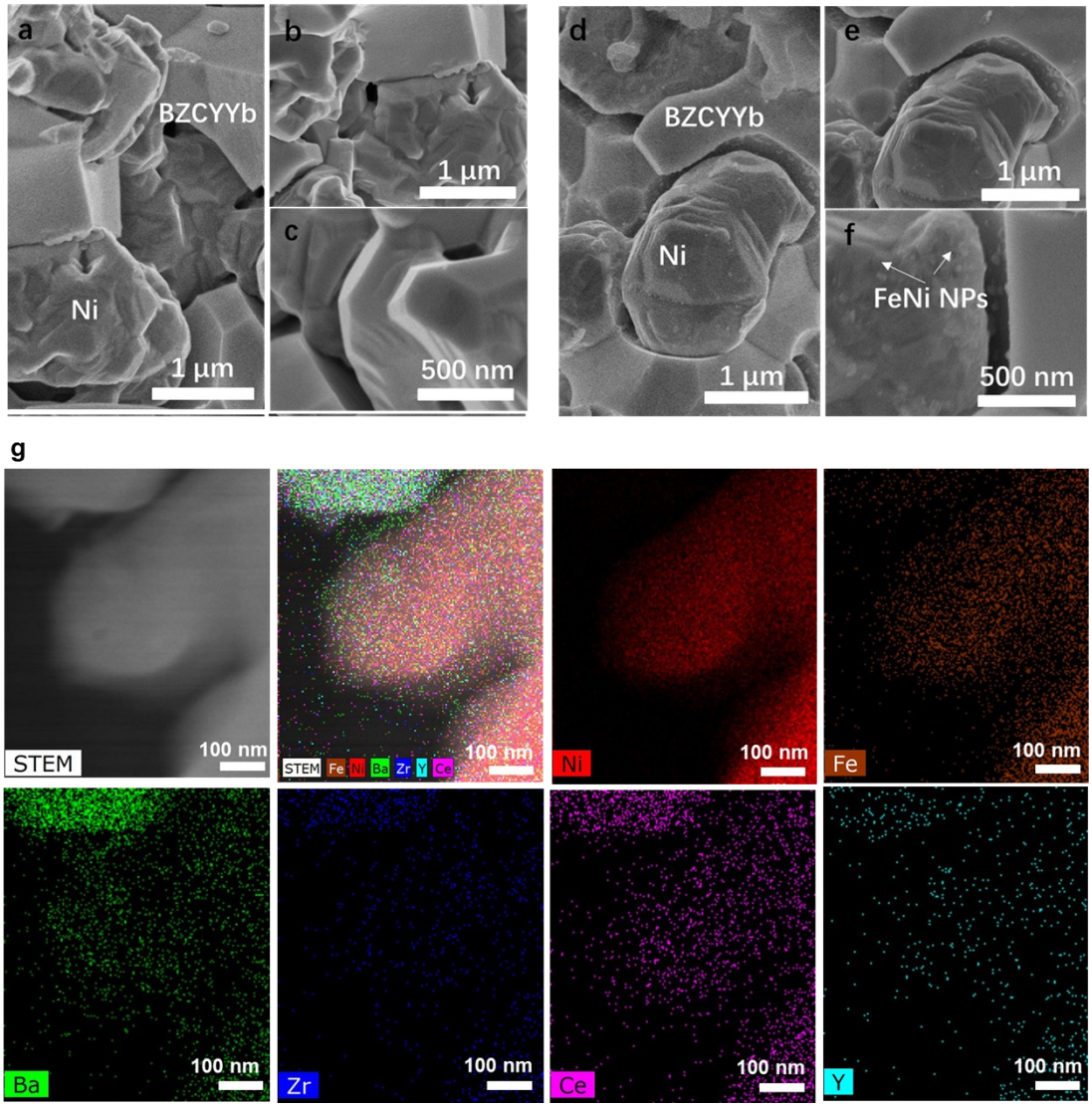

Supplementary Figure S3. Microstructure of NiO-BZCYYb surface before (**a-c**) and after modification (**d-f**), and a detailed STEM-EDX mapping (with a scale bar of 100 nm) of a Fe-modified Ni-BZCYYb anode (**g**). 10µL of 0.1M $Fe(NO_3)_3$ water solution was dispersed on the sintered NiO-BZCYYb surface followed by firing at 700°C in air for 3 h, then firing at 700°C in H_2 for 3 h. The NPs were mostly observed on the Ni surface rather than on the BZCYYb surface. This is also supported by the elemental mappings of energy-dispersive X-ray spectroscopy mapping (EDX, Figure 1).

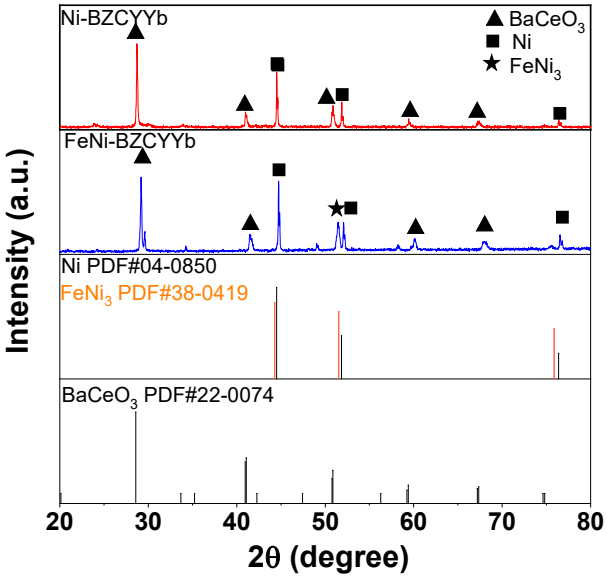

Supplementary Figure S4. XRD patterns of the Ni/BZCYYb anode (red) and Fe-modified Ni/BZCYYb anode (blue). It is suggested that an alloy with a composition of $FeNi_3$ is likely formed.

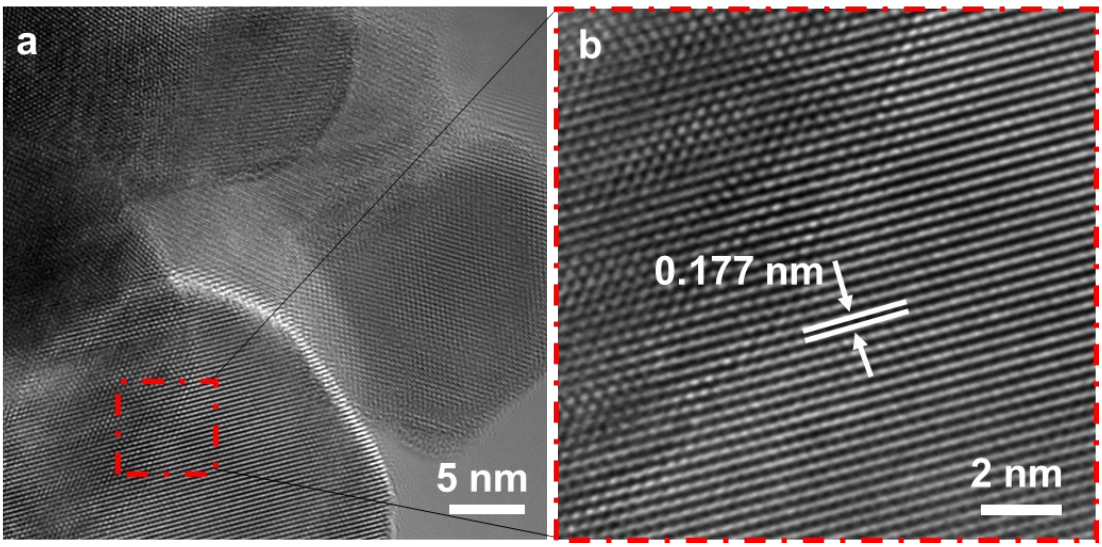

Supplementary Figure S5. A typical TEM image of the grain on anode surface. The lattice spacing of the surface coating is ~0.177 nm, likely corresponding to the (200) plane of the $FeNi_3$ alloy (PDF#38-0419)

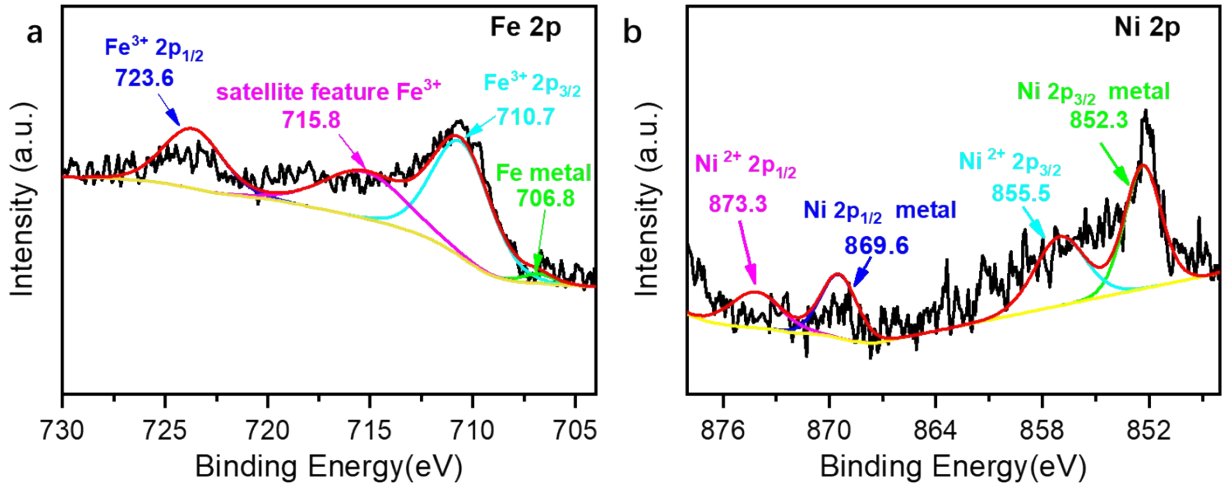

Supplementary Figure S6. High-resolution XPS spectra. (a) Fe 2p and (b) Ni 2p of reduced FeNi-BZCYYb anode.

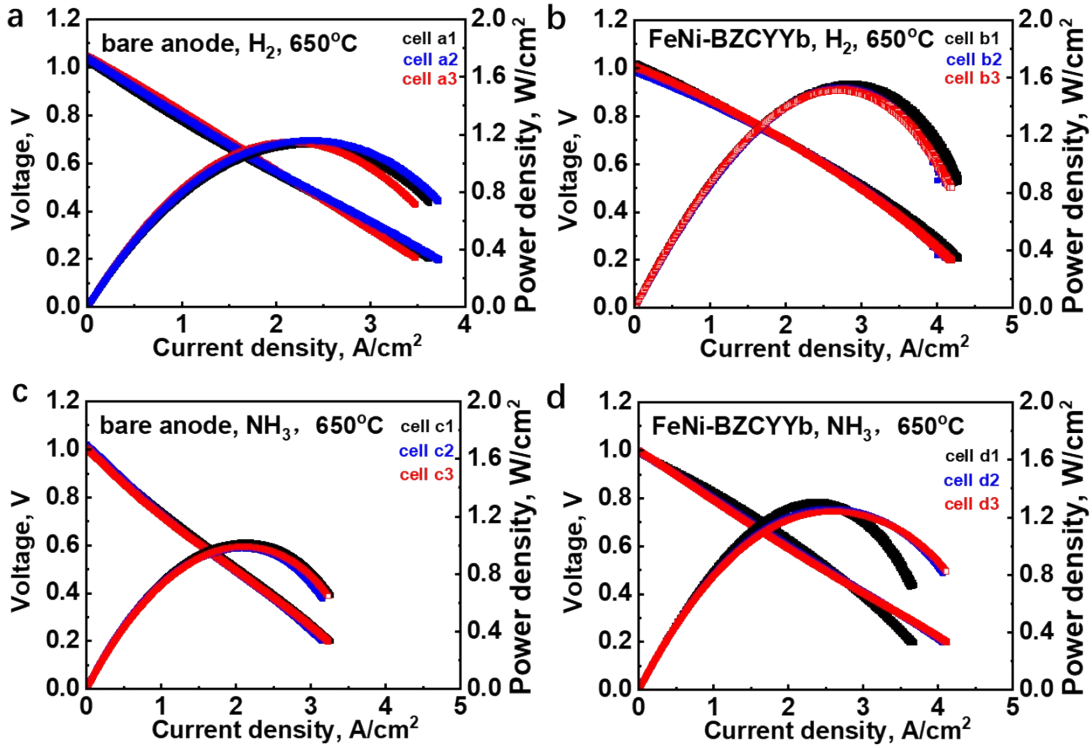

Supplementary Figure S7. Reproducibility testing of cells with same configuration. *IVP* curves of three independent single cells with bare Ni-BZCYYb anode tested at 650 °C using wet H_2 (3% humidity) (a) or dry ammonia (c) as fuel and ambient air as oxidant; *IVP* curves of three independent single cells tested with Fe-Ni-BZCYYb anode at 650 °C using wet H_2 (3% humidity) (b) or dry ammonia (d) as fuel and ambient air as oxidant.

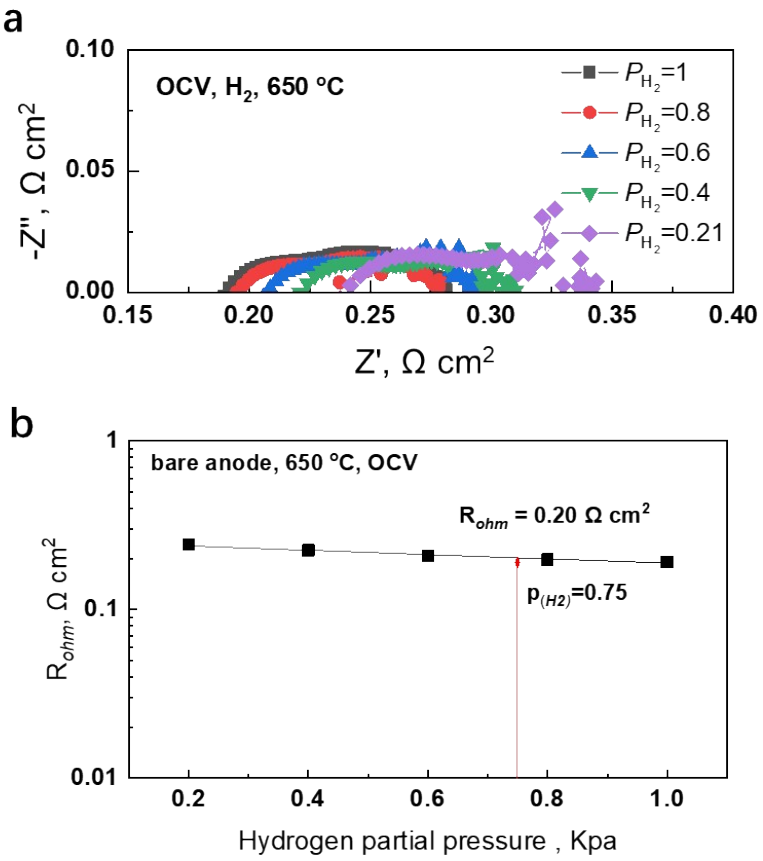

Supplementary Figure S8. (a) EIS of a single cell operated at various hydrogen partial pressure (p_{H_2} = 0.21 -1) in the bare anode at 650 °C, (b) the ohmic resistance dependency of hydrogen partial pressure in the bare anode at 650 °C.

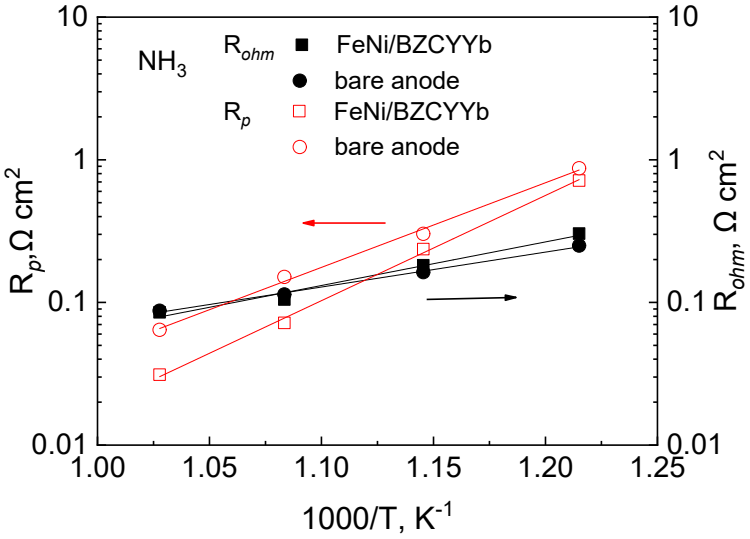

Supplementary Figure S9. Arrhenius plot of the electrode polarization resistance (R*p*) and R_{ohm} for the bare anode and Fe-modified Ni/BZCYYb anode, tested at 550–700 °C using ammonia as fuel and ambient air as oxidant.

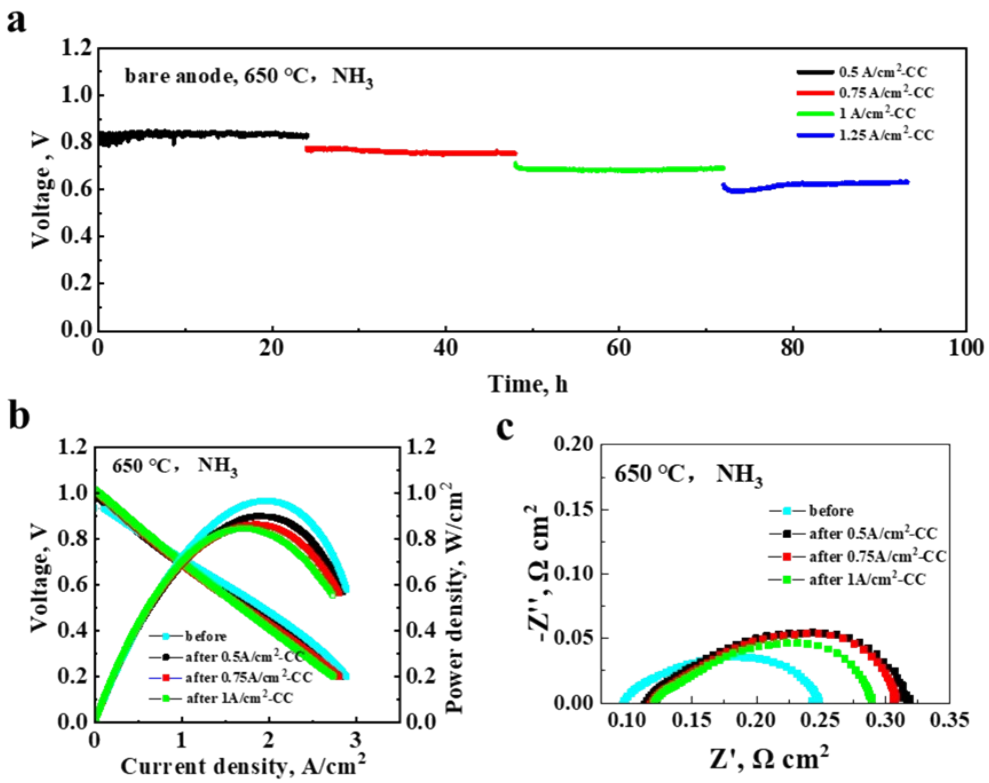

Supplementary Figure S10. Short-term stability test (24h) of the single cell on NH_3 fuel at 650 °C at a variable current density from 0.5 A cm^{-2} to 1.25 A cm^{-2}; (b) Typical *IV* and *IP* curves of the cell before and after short-term stability test at 0.5 A cm^{-2}, 0.75 A cm^{-2}, 1.0 A cm^{-2}; (c) Typical EIS of single cell before and after short-term stability test at 0.5 A cm^{-2}, 0.75 A cm^{-2}, and 1.0 A cm^{-2}, respectively.

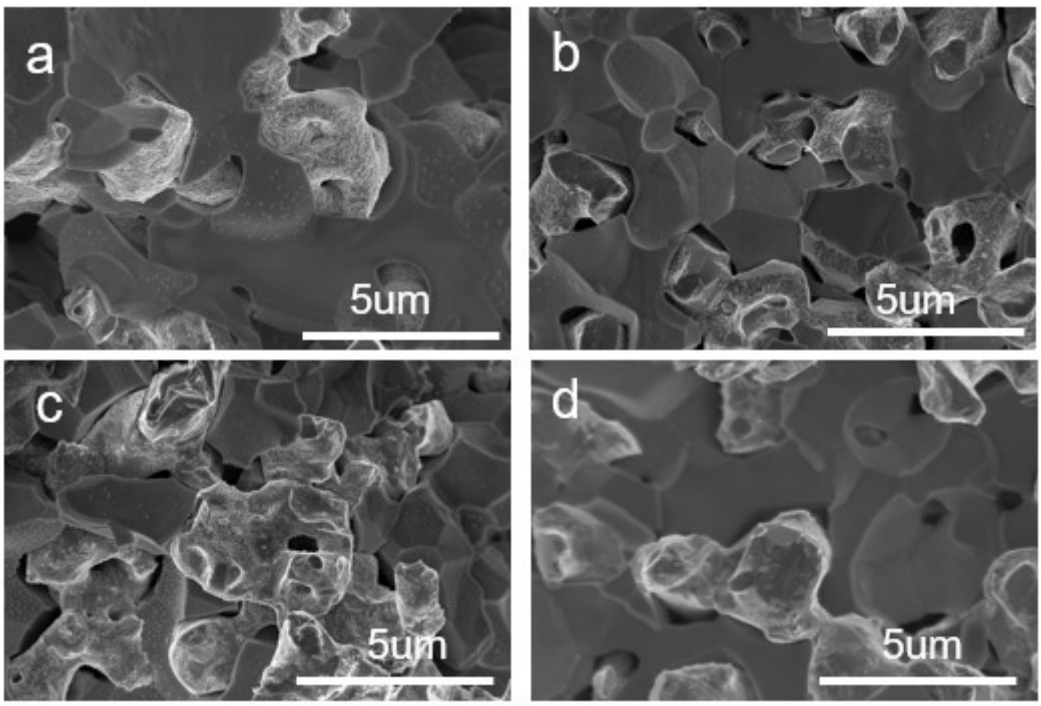

Supplementary Figure S11. Cross-sectional SEM images of reduced Ni/BZCYYb (a) before and (b) after a long-term durability test under wet H_2 (3% humidity) fuel at 650 °C for 100h, (c) SEM cross-sectional images of reduced Ni/BZCYYb after a further treatment under NH_3 fuel at 650 °C for 100h, (d) SEM cross-sectional images of Ni/BZCYYb anode infiltrated with 10μL of 0.1 mol L^{-1} $Fe(NO_3)_3$ after a further treatment under NH_3 fuel at 650 °C for 100h.

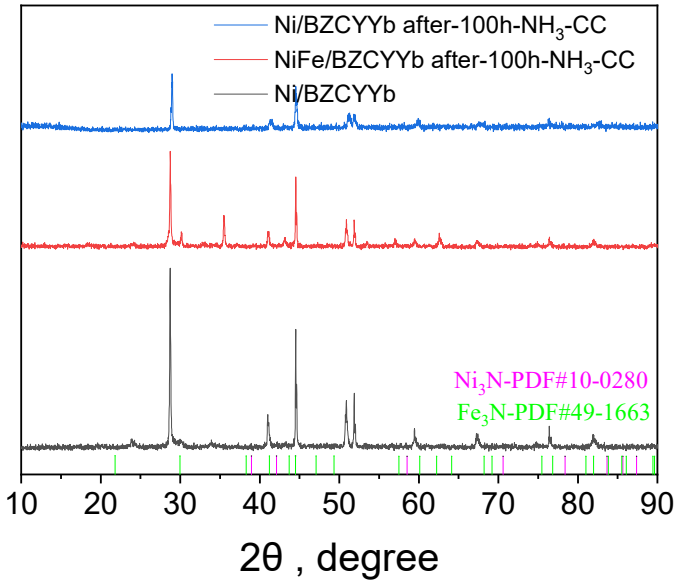

Supplementary Figure S12. XRD patterns for the bare anode and FeNi/BZCYYb anode before and after exposure to NH_3 at 650 °C for 100 h. Thermodynamic calculations for NiO reduction by H_2 and NH_3, and Ni_3N formation via NH_3 gas and metallic Ni. The figure shows that NH_3 is a stronger reducing agent than H_2 at temperatures exceeding 275 °C, and that Ni_3N formation is thermodynamically unfavorable under typical PCFC operation temperatures[13].

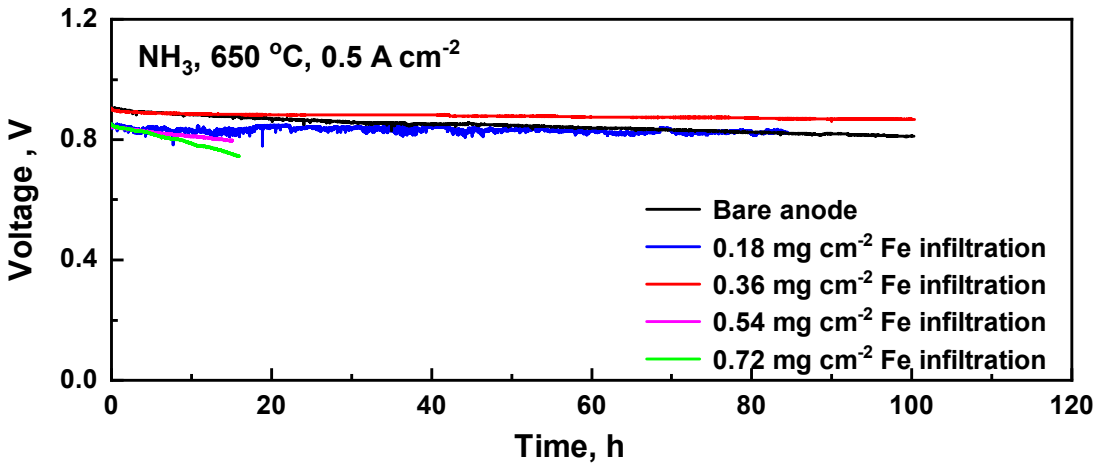

Supplementary Figure S13. Operation stability of the single cells at a constant current density of 0.5 A cm^{-2} at 650 °C in NH_3 fuel: with bare Ni/BZCYYb anode (black line), with 5μL (~0.18 mg cm^{-2}) Fe-modified Ni-BZCYYb anode (blue line), with 10μL (~0.36 mg cm^{-2}) Fe-modified Ni-BZCYYb anode (red line), with 15μL (~0.54 mg cm^{-2}) Fe-modified Ni-BZCYYb anode (purple line), with 20μL (~0.72 mg cm^{-2}) Fe-modified Ni-BZCYYb anode (green line)

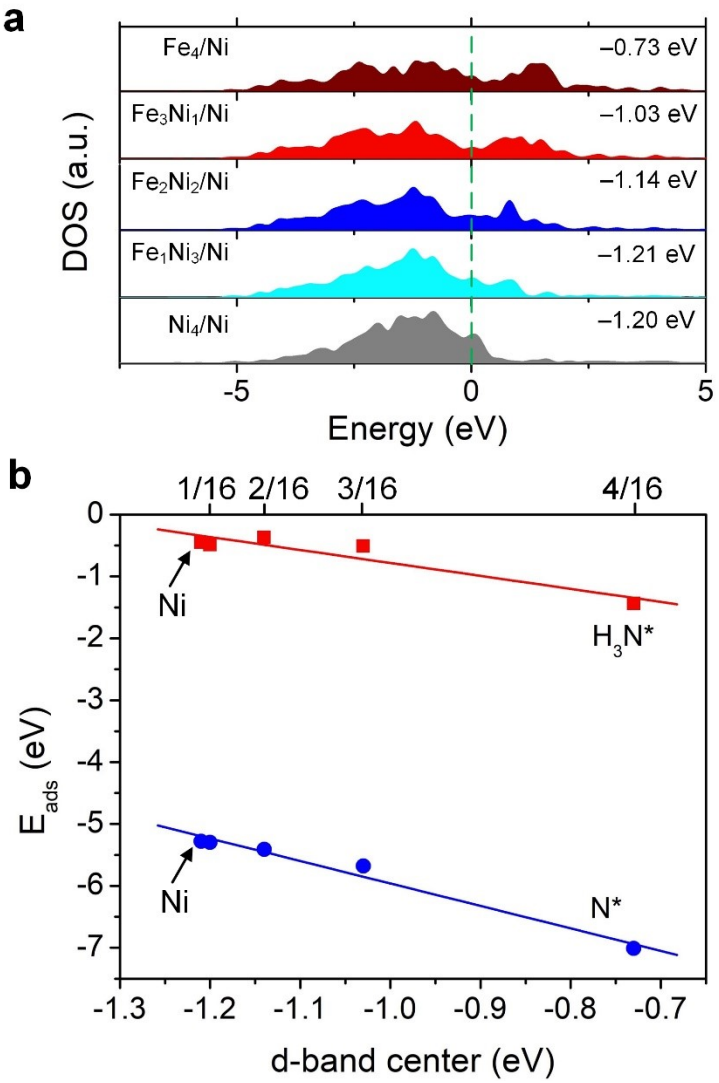

Supplementary Figure S14. (a) Calculated surface d-band density of states (DOS) for (2 × 2) four-layer Ni (111) (16 Ni; Ni_4/Ni) and FeNi (111) (Fe_1Ni_3/Ni, Fe_2Ni_2/Ni, Fe_3Ni_1/Ni, Fe_4/Ni). (b) Adsorption energies of H_3N* and N* against d-band centers. 1/16, 2/16, 3/16, and 4/16 are the concentration of Fe in Ni (Fe atoms/(Ni + Fe) atoms) (Fe_1Ni_3/Ni, Fe_2Ni_2/Ni, Fe_3Ni_1/Ni, and Fe_4/Ni, respectively).

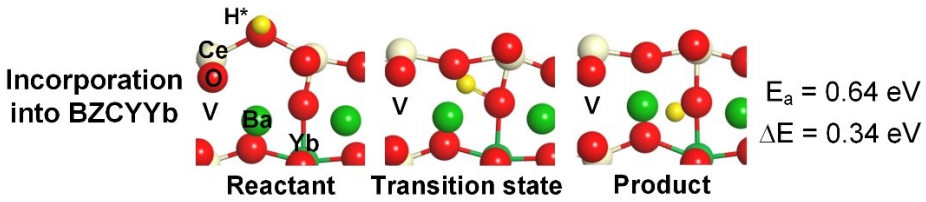

Supplementary Figure S15. Schematic of the incorporation of hydrogen species into BZCYYb (001) with a reaction barrier of 0.64 eV and its reaction energy of 0.34 eV which are not ZPE-corrected "V" represents an oxygen vacancy. The surface model with an oxygen vacancy formation energy with 0.28 eV was used.

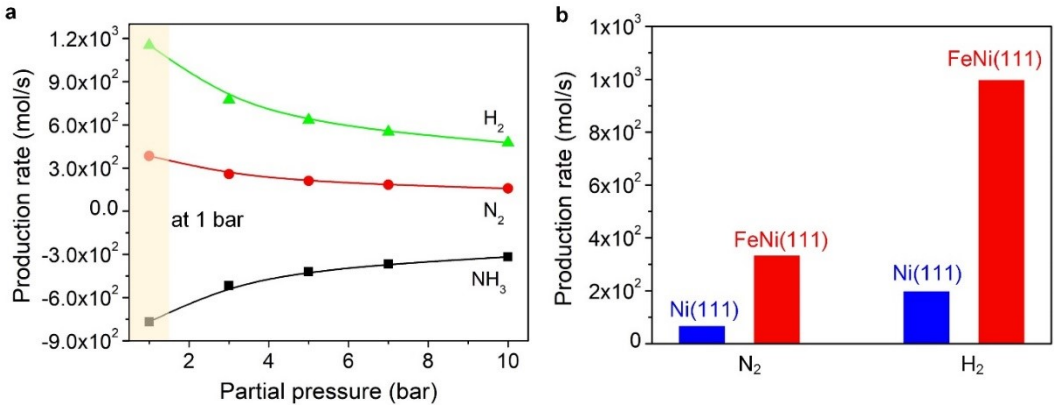

Supplementary Figure S16. Microkinetic modeling for the NH_3 decomposition. (a) Production rates of N_2 and H_2 (positive) and consumption rates of NH_3 (negative) as a function of partial pressures on Ni (111) at 700°C and (b) Production rates of N_2 and H_2 on Ni (111) and FeNi (111) at T = 700°C and P = 1bar. They were scaled by the PCFC's NH_3 utilization of ~17% in this study.

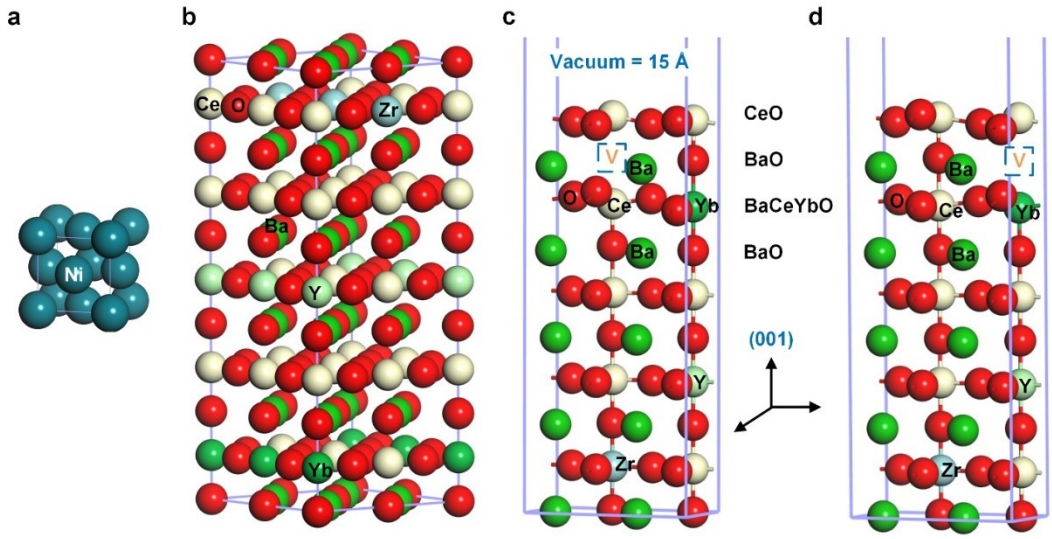

Supplementary Figure S17. The bulk structures of (a) Ni ($Fm\bar{3}m$; 225) with a = 3.5156 Å at GGA-PBE and (b) $BaZr_{0.7}Ce_{0.1}Y_{0.1}Yb_{0.1}O_3$ (BZCYYb) at GGA-PBE+U. The optimized lattice constants of BZCYYb are a = 4.4221 Å generated using the bulk structure of $BaCeO_3$ (BCO, $Pm\bar{3}m$; 221) with a = 4.4705 Å. (c), (d) 10-layer surface models used for the adsorption of hydrogen species (H*) and its incorporation into the bulk ($BaZr_{0.7}Ce_{0.1}Y_{0.1}Yb_{0.1}O_{3-\delta}$ (001)). "V" represents an oxygen vacancy. Its calculated surface energy is 0.39 J/m^3, while oxygen vacancy formation energies of the two surface models ((a) and (b)) are 0.22 eV and 0.28 eV, respectively.

Supplementary Table

Supplementary Table S1. Reproducibility data for the cells with same materials and configuration. Cells with bare Ni-BZCYYb anode tested at 650 °C using wet H_2 (3% humidity) (cell a1, a2, and a3) or dry ammonia (cell c1, c2, and c3) as fuel and ambient air as oxidant; cells with Fe-Ni-BZCYYb anode tested at 650 °C using wet H_2 (3% humidity) (cell b1, b2, and b3) or dry ammonia (cell d1, d2 and d3) as fuel and ambient air as oxidant.

	Bare anode, H_2			**Bare anode, NH_3**	
	OCV (V)	**MPD (W cm^{-2})**		**OCV (V)**	**MPD (W cm^{-2})**
cell a1	1.025	1.13	cell c1	1.01	1.019
cell a2	1.04	1.15	cell c2	1.003	0.991
cell a3	1.039	1.15	cell c3	1.021	0.978
	FeNi/BZCYYb anode, H_2			**FeNi/BZCYYb anode, NH_3**	
	OCV (V)	**MPD (W cm^{-2})**		**OCV (V)**	**MPD (W cm^{-2})**
cell b1	1.014	1.55	cell d1	0.989	1.3
cell b2	1.007	1.52	cell d2	0.993	1.256
cell b3	1.004	1.53	cell d3	0.998	1.24

Supplementary Table S2. Performance comparison of SOFCs (with difference materials or configurations) when operated with ammonia.

Electrolyte	Cathode	Anode	Electrolyte thickness [μm]	Fuel	Temp. [°C]	OCV[V]	Cell performance [mW cm^{-2}]	Year[Ref]
BZCYYb	PBSCF	Ni/BZCYYb	10	NH_3	700	0.99	1398	This work
					650	1.01	1020	
					600	1.029	691	
					550	1.015	332	
BZCYYb	PBSCF	Ni-Fe/BZCYYb	10	NH_3	700	0.96	1609	This work
					650	0.99	1257	
					600	1.019	723	
					550	1.034	360	
BCGO	$La_{0.5}Sr_{0.5}CoO_{3-\delta}$ (LSCO)–BCGO	Ni-$BaCe_{0.8}Gd_{0.2}O_{2.9}$ (BCGO)	50	NH_3	750	0.985	384	2007[26]
					700	0.995	355	
					650	1.095	184	
					600	1.102	96	
SDC	$Ba_{0.5}Sr_{0.5}Co_{0.8}Fe_{0.2}O_{3-\delta}$(BSCF)	NiO	10	NH_3	650	0.768	1190	2007[27]
					600	0.771	434	
					550	0.795	167	
BCNO	$La_{0.5}Sr_{0.5}CoO_{3-\delta}$(LSCO)	Ni-$BaCe_{0.9}Nd_{0.1}O_{3-\delta}$ (BCNO)	20	NH_3	700	0.95	315	2007[28]
$BaCe_{0.8}Gd_{0.2}O_{3-\delta}$ (BCGO)	$Ba_{0.5}Sr_{0.5}Co_{0.8}Fe_{0.2}O_{3-\delta}$(BSCF)-CGO	Ni-$Ce_{0.8}Gd_{0.2}O_{1.9}$ (CGO)	30	NH_3	600	1.1	147	2008[29]
					650	1.12	200	
$BaCe_{0.8}Gd_{0.15}Pr_{0.05}O_3$ (BCGP)	Pt	Ni-$BaCe_{0.85}Eu_{0.15}O_3$(BCE)	50	NH_3	600		28	2010[30]
					550	0.92	18	
					500		15	
Ni-$BaZr_{0.1}Ce_{0.7}Y_{0.2}O_{3-\delta}$ (BZCY)	$Ba_{0.5}Sr_{0.5}Co_{0.8}Fe_{0.2}O_{3-\delta}$ (BSCF)	BZCY	35	NH_3	750		390	2015[31]
					700		325	
					650		275	
					600	0.98	190	
					550		125	
					500		65	
					450		25	
BZY	Pt	Ni-BZY	60-90	NH_3	700	0.8	130	2017[32]
					650	0.87	96	
					600	0.92	70	
ScCSZ	Pt	Pt	1000	6%NH_3 /Ar	900	0.9	7.2	2018[33]
ScCSZ	$Sm_{0.5}Sr_{0.5}CoO_{3d}$	40wt%	1000	6%NH_3	900	1.1	98.8	2018[34]

	(SSC)–$(SmO_{1.5})_{0.2}(CeO_2)_{0.8}$ (SDC)	Ni -SDC		/Ar	850	1.15	70	
					800	1.15	45	
					750	1.15	20	
		10 wt% Ni–SDC	1000	6%NH_3 /Ar	750	1.15	96.5	
		50 wt% Ni–SDC	1000	6%NH_3 /Ar	750	1.09	67.7	
YSZ	LSC/GDC	Ni/YSZ	3	NH_3	750	1.05	950	2018[35]
					800	1.05	1078	
					850	1.05	1174	
BZCY	$La_{0.6}Sr_{0.4}Co_{0.2}Fe_{0.8}O_{3-d}$ (LSCF)	Pd	1	NH_3	600	0.95	580	2018[12]
					550	1	340	
					500	1.03	210	
					450	0.98	71	
YSZ	LSCF	Ni/YSZ	10	NH_3	750		584	2019[36]
YSZ	$La_{0.6}Sr_{0.4}Co_{0.2}Fe_{0.8}O_{3-d}$ (LSCF)	Ba-Ni/YSZ	10	NH_3	650	1.18	125	2020[37]
					700	1.17	225	
					750	1.14	275	
SDC	$Ba_{0.5}Sr_{0.5}Co_{0.8}Fe_{0.2}O_{3-\delta}$ (BSCF)	NiCo-$La_{0.55}Sr_{0.30}TiO_{3-\delta}$(LST)-SDC	350	NH_3	650	0.87	120	2020[38]
					700	0.86	190	
					750	0.82	260	
					800	0.81	361	
SDC	$Ba_{0.5}Sr_{0.5}Co_{0.8}Fe_{0.2}O_{3-\delta}$ (BSCF)	Ni/Co-LSTN	350	NH_3	800	0.81	161	
SDC	$Ba_{0.5}Sr_{0.5}Co_{0.8}Fe_{0.2}O_{3-\delta}$ (BSCF)	Ni/Co-LSTC	350	NH_3	800	0.81	98	
YSZ	LSCF/GDC	Ni/YSZ	10	NH_3	750	1.03	195	2020[39]
BCY20	BCY20-LSCF	Ni-BCZY	50-60	NH_3	700	1.06	340	2020[40]
					650	1.08	240	
					600	1.10	180	
					550	1.12	130	
BZCYYb	BCFZY	Ni-BZCYYbPd	20	NH_3	650	1.02	600	2021[41]
					600	1.05	440	
					550	1.1	336	

Supplementary Table S3. A list of studies that have reported long-term operations of SOFC on NH_3.

Cell structure/sample details	Temperature/duration	Fuel composition	Performance/current density	Remarks	Year[Ref]
monolithic BCE fuel cell: $BaCe_{0.85}Eu_{0.15}O_3$, BCE electrolyte. Engelhard platinum ink A-4338 for the anode and cathode.	700 °C/200 h	NH_3	~30 mW cm^2	no detectable decay in performance	2006 [42]
Ni–SDC/ SDC (50 μm) / SSC–SDC	600 °C/50 h	NH_3	0.45 V at a current density of 360 mA cm^2	no detectable decay in performance	2006 [43]
an anode-supported tubular anode NiO-YSZ/8YSZ/GDC/LSCF	800 °C/100 h	NH_3	0.68 V at a current density of 242 mA cm^2	no deterioration in performance	2007 [44]
a commercial microtubular SOFC (Adelan) Ni/YSZ /YSZ/ LSM	700 -900°C /51h	humidified NH_3	0.6 V at a current density of 100 mA cm^2	no detectable decay in performance	2009 [45]
Ni-YSZ/Ni-SSZ/SSZ/SSZ-LSM	750 °C/2 h	NH_3	~626 mW cm^2	no detectable decay in performance	2012 [46]
SOFC stacks	770 °C/1000 h	NH_3	200 W	the decrease in voltage was around 10%	2017 [47]
Ni–YSZ|YSZ|GDC|LSCF	600 °C/235 h	66.67% NH_3-1.67% H_2O-31.67% N_2	~240 mW cm^2	3%/100h	2017[48]
Ni–8YSZ cermet anode and 8YSZ electrolyte (ASC-Planar)	750 °C/100 h	NH_3	0.81 V at a current density of 500 mA/cm^2	voltage degradation decay 1.5%/100h.	2019 [49]

a flat-tube SOFC with symmetric double-sided cathodes Ni–YSZ|YSZ|GDC|LSCF	750 °C /120h	66.7% NH_3– 33.3% N_2	~0.8 V at a current density of 200 mA cm^2	a slight decrease in the voltage	2020 [39]
SOFC stacks	840 °C/1000 h	humidified ammonia	~181 mW cm^2	no apparent ammonia caused degradation	2020 [50]
Ni-BZCYYbPd|BZCYYbPd|BCFYZ	550 °C /130h	NH_3	~0.76 V at a current density of 200 mA cm^2	dropped by only 0.01 V after 130 h	2021[41]
~500 μm Ni-BCZYYb/ ~4 μm BCZYYbN ($BaCe_{0.7}Zr_{0.1}Y_{0.1}Yb_{0.1}Ni_{0.04}O3-\delta$)/ a ~20 μm BCFZY ($BaCo0.4Fe_{0.4}Zr_{0.1}Y_{0.1}O_{3-\delta}$)	650 °C /15h	NH_3	~0.78 V at a current density of 500 mA cm^2	the voltage dropped to zero	2021 [13]
Ni-BZCYYb|BZCYYb|PBSCF	650 °C /100h	NH_3	~0.9 V at a current density of 500 mA cm^2	0.008 V h^{-1}	This work
NiFe-BZCYYb|BZCYYb|PBSCF	650 °C /100h	NH_3	~0.9 V at a current density of 500 mA cm^2	0.0022 V h^{-1}	This work

Supplementary Table S4. Absorption sites and adsorption energies (eV) of surface species on Ni (111) and Fe (110).[1]

species	Ni (111)		Fe (110)	
	active site	E_{ads} (eV)	active site	E_{ads} (eV)
H_3N*	atop	–0.75	atop	–0.83
H_2N*	bridge	–2.73	bridge	–3.17
HN*	fcc	–4.57	hollow	–5.49
N*	fcc	–5.30	hollow	–6.61
H*	hcp	–2.81	hcp	–2.77

[1] Reference: Duan, X.; Ji, J.; Qian, G.; Fan, C.; Zhu, Y.; Zhou, X.; Chen, D.; Yuan, W., "Ammonia decomposition on Fe (110), Co (111) and Ni (111) surfaces: A density functional theory study," *Journal of Molecular Catalysis A: Chemical*, 357, 81-86 (2012).

Supplementary Table S5. Compilation of absorption sites and adsorption energies[1] (eV) of surface species on Ni (111) and FeNi (111).

species	Ni (111)		FeNi (111)	
	active site	E_{ads} (eV)	active site	E_{ads} (eV)
H_3N*	atop	–0.68	atop on Fe	–0.71
H_2N*	bridge	–2.70	bridge between Ni and Fe	–2.74
HN*	fcc	–4.54	fcc linked two Ni and the Fe atoms	–4.57
N*	fcc	–5.27	fcc on three Ni atoms	–5.26
H*	hcp	–2.80	hcp on three Ni atoms	–2.80

[1] The adsorption energies are before adding the zero-point energy (ZPE) correction.

Supplementary Table S6. Compilation of ZPE-corrected relative energies on Ni (111) an FeNi (111) used for mechanistic and kinetic studies.

Reaction	Ni (111)			FeNi (111)		
	E (eV)	$E_{,ZPE}$ (eV)	E_{rel} (eV)	E (eV)	$E_{,ZPE}$ (eV)	E_{rel} (eV)
NH_3 decomposition						
NH_3(g) + surface	–208.6239	–207.5625	0.00	–211.6002	–210.5500	0.00
H_3N*	–209.2999	–208.1327	–0.57	–212.3109	–211.1524	–0.60
TS2	–207.8513	–206.9061	0.66	–211.0896	–210.1853	0.36
H_2N* + H*	–209.2358	–208.2356	–0.67	–212.2632	–211.2567	–0.71
TS3	–208.4897	–207.7174	–0.15	–211.4883	–210.7054	–0.16
NH* + 2H*	–209.5572	–208.6840	–1.12	–212.5759	–211.7145	–1.16
TS4	–208.2112	–207.8719	–0.31	–211.2338	–210.5567	–0.01
N* + 3H*	–209.2235	–208.4635	–0.90	–212.2135	–211.4657	–0.92
N_2 formation						
N* + N*	–205.8786	–205.4961	0.00	–208.8339	–208.4670	0.00
TS5	–203.8831	–203.5781	1.92	–206.9664	–206.6637	1.80
N_2(g)	–205.7104	–205.4084	0.09	–208.6867	–208.3959	0.07
H_2 formation						
H* + H*	–196.9215	–196.4414	0.00	–199.9139	–199.4442	0.00
H_2(g)	–195.8602	–195.4410	1.00	–198.8365	–198.4285	1.02
Surface diffusion of atomic hydrogen						
H_{fcc}*	–193.0097	–192.6940	0.00	–195.9941	–195.6892	0.00
$TS_{diffusion}$	–192.8655	–192.5716	0.12	–195.8434	–195.5635	0.13
H_{hcp}*	–192.9966	–192.6962	0.00	–195.9712	–195.6789	0.01

Supplementary Table S7. Reaction mechanisms, pre-exponential factors (A_i) calculated at 700°C, and rate constants (k_i) applied for microkinetic modeling on Ni (111) and FeNi (111).

No.	Ni (111)	forward reaction		reverse reaction	
		A_i (s^{-1})	k_i (s^{-1})	A_i (s^{-1})	k_i (s^{-1})
R1	$NH_3(g) + * \leftrightarrow H_3N*$	4.24×10^{11}	4.53×10^{11}	8.03×10^{14}	9.53×10^{11}
R2	$H_3N* + * \leftrightarrow H_2N* + H*$	9.49×10^{13}	4.23×10^{7}	5.14×10^{14}	6.66×10^{7}
R3	$H_2N* + * \leftrightarrow HN* + H*$	2.11×10^{12}	4.37×10^{9}	6.40×10^{13}	6.27×10^{8}
R4	$HN* + * \leftrightarrow N* + H*$	3.08×10^{12}	1.90×10^{8}	1.83×10^{12}	1.57×10^{9}
R5	$N* + N* \leftrightarrow N_2(g) + 2*$	8.87×10^{12}	$1.03\times \quad 10^{3}$	9.78×10^{9}	3.24
R6	$H* + H* \leftrightarrow H_2(g) + 2*$	5.97×10^{7}	5.97×10^{7}	7.19×10^{14}	4.75×10^{9}

No.	FeNi (111)	forward reaction		reverse reaction	
		A_i (s^{-1})	k_i (s^{-1})	A_i (s^{-1})	k_i (s^{-1})
R1	$NH_3(g) + * \leftrightarrow H_3N*$	8.66×10^{10}	1.03×10^{11}	6.90×10^{16}	6.24×10^{13}
R2	$H_3N* + * \leftrightarrow H_2N* + H*$	8.12×10^{12}	7.96×10^{7}	1.28×10^{14}	3.60×10^{8}
R3	$H_2N* + * \leftrightarrow HN* + H*$	9.28×10^{12}	1.29×10^{10}	1.46×10^{13}	8.62×10^{7}
R4	$HN* + * \leftrightarrow N* + H*$	6.21×10^{12}	6.26×10^{6}	1.81×10^{13}	3.55×10^{8}
R5	$N* + N* \leftrightarrow N_2(g) + 2*$	1.24×10^{13}	5.66×10^{3}	6.24×10^{9}	2.52
R6	$H* + H* \leftrightarrow H_2(g) + 2*$	5.97×10^{7}	5.97×10^{7}	7.19×10^{14}	3.94×10^{9}

An "*" represents a free site on the surface. **R1**, **R2**, **R3**, **R4**, and **R5** were described using the Arrhenius equation, while **R6** was using the Hertz-Knudsen expression (see below).

$$k_{ads} = \frac{PA}{\sqrt{2\pi m k_B T}}$$

where P is the partial pressure of the gas-phase molecule and A is the area of the surface site. The kinetic parameters for the adsorption and desorption steps of H_2 are summarized as follows.

Species	A (m^2)	m (amu)	σ	θ_{rot} (K)	E_{des} (eV)
H_2	area	molecular mass	symmetry number	characteristic temperature for rotation	desorption energy
	1×10^{-20}	2	2	87.6	1.00 (Ni (111)) 1.02 (FeNi (111))

Supplementary Table S8. Production rates[1] at T = 700°C and P = 1bar on Ni (111) and FeNi (111) via microkinetic modeling.

	N_2 (mol/s)	H_2 (mol/s)
Ni (111)	65.3	196.0
FeNi (111)	331.8	995.5

[1] The rate was scaled by an experimentally measured fuel utilization of NH_3 summarized in the **Supplementary Note 16**: Fuel utilization of ~17%.

Supplementary References

1. G. Kresse and J. Furthmuller, *Phys. Rev. B*, 1996, **54**, 11169-11186.
2. G. Kresse and J. Hafner, *Phys Rev B Condens Matter*, 1993, **47**, 558-561.
3. J. P. Perdew, K. Burke and M. Ernzerhof, *Phys. Rev. Lett.*, 1996, **77**, 3865-3868.
4. G. Kresse and D. Joubert, *Phys. Rev. B*, 1999, **59**, 1758-1775.
5. Y. Choi, M. Scott, T. Sohnel and H. Idriss, *Phys. Chem. Chem. Phys.*, 2014, **16**, 22588-22599.
6. X. F. Yang, L. C. Jia, B. C. Pan, B. Chi, J. Pu and J. Li, *J. Phys. Chem. C*, 2020, **124**, 8024-8033.
7. G. Henkelman, B. P. Uberuaga and H. Jonsson, *J. Chem. Phys.*, 2000, **113**, 9901-9904.
8. I. A. Filot, R. A. van Santen and E. J. Hensen, *Angew. Chem. Int. Ed. Engl.*, 2014, **53**, 12746-12750.
9. C. Han, H. Zhang, D. Zhang, Y. Deng, J. Shen and G. Zeng, *Nanomaterials (Basel)*, 2020, **10**.
10. J. Feng, Y. Zong, Y. Sun, Y. Zhang, X. Yang, G. K. Long, Y. Wang, X. H. Li and X. L. Zheng, *Chem. Eng. J.*, 2018, **345**, 441-451.
11. P. Jing, M. Liu, Y. Pu, Y. Cui, Z. Wang, J. Wang and Q. Liu, *Sci Rep*, 2016, **6**, 37701.
12. Y. Aoki, T. Yamaguchi, S. Kobayashi, D. Kowalski, C. Zhu and H. Habazaki, *Global Challenges*, 2018, **2**, 1700088.
13. L. Z. Zhu, C. Cadigan, C. C. Duan, J. K. Huang, L. Z. Bian, L. Le, C. H. Hernandez, V. Avance, R. O'Hayre and N. P. Sullivan, *Communications Chemistry*, 2021, **4**.
14. A. Hagen, H. Langnickel and X. F. Sun, *Int. J. Hydrogen Energy*, 2019, **44**, 18382-18392.
15. J. Yang, A. F. Molouk, T. Okanishi, H. Muroyama, T. Matsui and K. Eguchi, *ACS Appl Mater Interfaces*, 2015, **7**, 28701-28707.
16. M. Kishimoto, H. Muroyama, S. Suzuki, M. Saito, T. Koide, Y. Takahashi, T. Horiuchi, H. Yamasaki, S. Matsumoto, H. Kubo, N. Takahashi, A. Okabe, S.

Ueguchi, M. Jun, A. Tateno, T. Matsuo, T. Matsui, H. Iwai, H. Yoshida and K. Eguchi, *Fuel Cells*, 2020, **20**, 80-88.

17. G. Kresse and D. Joubert, *Phys Rev B*, 1999, **59**, 1758-1775.
18. H. J. Monkhorst and J. D. Pack, *Phys. Rev. B*, 1976, **13**, 5188-5192.
19. T. Tauer, R. O'Hayre and J. W. Medlin, *J. Mater. Chem. A* 2013, **1**, 2840-2846.
20. M. Shishkin and T. Ziegler, *Surf. Sci.*, 2012, **606**, 1078-1087.
21. Z. Yang, T. K. Woo, M. Baudin and K. Hermansson, *J. Chem. Phys.*, 2004, **120**, 7741-7749.
22. A. Nilsson, L. G. M. Pettersson, B. Hammer, T. Bligaard, C. H. Christensen and J. K. Norskov, *Catal. Lett.*, 2005, **100**, 111-114.
23. K. J. Laidler, *Chemical Kinetics*, Harper and Row, New York, 3rd. edn., 1987.
24. D. G. Truhlar, *The Reaction Path in Chemistry: Current Approaches and Perspectives;* , Kluwer Academic Publishers, The Netherlands, 1995.
25. Y. Choi, M. E. Lynch, M. C. Lin and M. Liu, *J. Phys. Chem. C.*, 2009, **113**, 7290-7297.
26. Q. L. Ma, R. R. Peng, Y. J. Lin, H. F. Gao and G. Y. Meng, *J. Power Sources*, 2006, **161**, 95-98.
27. G. Y. Meng, C. R. Jiang, J. J. Ma, Q. L. Ma and X. Q. Liu, *J. Power Sources*, 2007, **173**, 189-193.
28. K. Xie, Q. Ma, B. Lin, Y. Jiang, J. Gao, X. Liu and G. Meng, *J. Power Sources*, 2007, **170**, 38-41.
29. L. Zhang and W. Yang, *J. Power Sources*, 2008, **179**, 92-95.
30. Y. Lin, R. Ran, Y. M. Guo, W. Zhou, R. Cai, J. Wang and Z. P. Shao, *Int. J. Hydrogen Energy*, 2010, **35**, 2637-2642.
31. J., Yang, T., Akagi, T., Okanishi, H., Muroyama, T. and Matsui, *Fuel Cells*, 2015, **15**, 390-397.
32. K. Miyazaki, T. Okanishi, H. Muroyama, T. Matsui and K. Eguchi, *J. Power Sources*, 2017, **365**, 148-154.
33. Y. Itagaki, J. Cui, N. Ito, H. Aono and H. Yahiro, *J. Ceram. Soc. Jpn.*, 2018, **126**, 870-876.

34. J. C. Y. Itagaki, N. Ito, H. Aono, and H. Yahiro, *ECS Trans.*, 2018, **85**, 779-786.
35. S. S. Shy, S. C. Hsieh and H. Y. Chang, *J. Power Sources*, 2018, **396**, 80-87.
36. B. Stoeckl, V. Subotic, M. Preininger, M. Schwaiger, N. Evic, H. Schroettner and C. Hochenauer, *Electrochim. Acta*, 2019, **298**, 874-883.
37. Y. H. Wang, J. Yang, J. X. Wang, W. B. Guan, B. Chi, L. C. Jia, J. Y. Chen, H. Muroyama, T. Matsui and K. Eguchi, *J. Electrochem. Soc.*, 2020, **167**, 064501.
38. Y. Song, H. Li, M. Xu, G. Yang, W. Wang, R. Ran, W. Zhou and Z. Shao, *Small*, 2020, **16**, 2001859.
39. Y. Wang, Y. Gu, H. Zhang, J. Yang, J. Wang, W. Guan, J. Chen, B. Chi, L. Jia, H. Muroyama, T. Matsui, K. Eguchi and Z. Zhong, *Appl. Energy*, 2020, **270**, 115185.
40. K. Miyazaki, H. Muroyama, T. Matsui and K. Eguchi, *Sustain Energ Fuels*, 2020, **4**, 5238-5246.
41. F. He, Q. N. Gao, Z. Q. Liu, M. T. Yang, R. Ran, G. M. Yang, W. Wang, W. Zhou and Z. P. Shao, *Adv Energy Mater*, 2021, DOI: 10.1002/aenm.202003916, 2003916.
42. N. Maffei, L. Pelletier, J. P. Charland and A. McFarlan, *J. Power Sources*, 2006, **162**, 165-167.
43. Q. Ma, R. Peng, L. Tian and G. Meng, *Electrochem. Commun.*, 2006, **8**, 1791-1795.
44. L. Zhang, Y. Cong, W. Yang and L. Lin, *Chinese Journal of Catalysis*, 2007, **28**, 749-751.
45. A. Fuerte, R. X. Valenzuela, M. J. Escudero and L. Daza, *J. Power Sources*, 2009, **192**, 170-174.
46. L. Liu, K. Sun, X. Wu, X. Li, M. Zhang, N. Zhang and X. Zhou, *Int. J. Hydrogen Energy*, 2012, **37**, 10857-10865.
47. T. Okanishi, K. Okura, A. Srifa, H. Muroyama, T. Matsui, M. Kishimoto, M. Saito, H. Iwai, H. Yoshida, M. Saito, T. Koide, H. Iwai, S. Suzuki, Y. Takahashi, T. Horiuchi, H. Yamasaki, S. Matsumoto, S. Yumoto, H. Kubo, J. Kawahara, A. Okabe, Y. Kikkawa, T. Isomura and K. Eguchi, *Fuel Cells*, 2017,

17, 383-390.

48. H. M. V. Singh, T. Matsui, K. Eguchi *ECS Trans.*, 2017, **78**, 2527-2536.

49. G. Cinti, L. Barelli and G. Bidini, presented in part at the Second International Conference on Material Science, Smart Structures and Applications: Icmss-2019, 2019.

50. B. Stoeckl, M. Preininger, V. Subotić, S. Megel, C. Folgner and C. Hochenauer, *J. Power Sources*, 2020, **450**.